Valence band structure of ultrathin silicon and germanium channels in metal-oxide-semiconductor field-effect transistors

Tony Low, M. F. Li,[a] and Y. C. Yeo
Silicon Nano Device Laboratory (SNDL) Electrical and Computer Engineering (ECE) Department, National University of Singapore and Institute of Microelectronics, Singapore 119260, Singapore

W. J. Fan and S. T. Ng
Electrical and Computer Engineering (ECE) Department, Nanyang Technological University of Singapore, Singapore 63979 Singapore

D. L. Kwong
Electrical and Computer Engineering (ECE) Department, University of Texas, Austin, Texas 78712

(Received 8 September 2004; accepted 17 May 2005; published online 18 July 2005)

The ultrathin body (UTB) silicon-on-insulator metal-oxide-semiconductor field-effect transistor (MOSFET) is promising for sub-50-nm complementary metal-oxide semiconductor technologies. To explore a high-mobility channel for this technology, this paper presents an examination of Si and Ge hole sub-band structure in UTB MOSFETs under different surface orientations. The dependence of the hole subband structure on the film thickness (T_{Body}) was also studied in this work. We found that the valence-band mixing in the vicinity of the zone center Γ is strongly dependent on T_{Body} for both Si and Ge, particularly for the $\langle 110 \rangle$ surface orientation. This gives rise to the following two phenomena that crucially affect the electrical characteristics of *p*-MOSFETs: (1) an anomalous increase of quantization mass for $\langle 110 \rangle$ Si and Ge surfaces as T_{Body} is scaled below 5 nm. (2) The dependence of energy dispersion and anisotropy on T_{Body} especially for the $\langle 110 \rangle$ surface, which advantageously increases hole velocity along the [011] channel as T_{Body} is decreased. The density of states for different surface orientations are also calculated, and show that—for any given surface orientation—Ge has a smaller density of states than Si. The Ge $\langle 110 \rangle$ surface has the lowest density of states among the surface orientations considered. © *2005 American Institute of Physics*. [DOI: 10.1063/1.1948528]

I. INTRODUCTION

The ultrathin body (UTB) silicon-on-insulator (SOI) metal-oxide-semiconductor field-effect transistor (MOSFET) is a promising candidate for the development of sub-50-nm complementary metal-oxide semiconductor (CMOS) technologies.[1] However, recent experimental work[2,3] has reported serious mobility degradation in Si UTB MOSFETs with T_{Body} less than 5 nm. This may present significant limitations to achieving ballistic transport in Si UTB MOSFET devices[4,5] with a sub-10-nm gate length.[6,7] To counteract this problem, several notable efforts are being made to implement a higher mobility channel. Ge UTB *p*-MOSFET devices with a T_{Body} of 4.5 nm have been fabricated using the local condensation techniques,[8] with large mobility improvement over Si MOSFETs. The technology for fabricating *n*-MOSFET and *p*-MOSFET devices on hybrid substrates[9] along their optimum surfaces and channel orientations has also been demonstrated.[9] To further this effort, it is of paramount importance to understand the band-structure characteristics of these thin-film channels, especially for the case of complicated valence bands. In the dissipative transport regime, it is advantageous to select and orient the band structure to yield a smaller two-dimensional (2D) density-of-states mass (m_D) and conductivity mass (m_C).[10] However, from a current overdrive point of view,[11] a larger m_D is more desirable. A large quantization mass (m_Z) is also pertinent for the suppression of surface-roughness scattering for UTB MOSFETs with a sub-5-nm T_{Body}.[12]

The purpose of this article is to provide a detailed examination of the impact of T_{Body} on the hole subband structure of Si and Ge with sub-10-nm T_{Body} and discuss its implications for carrier transport attributes in its relation to their effective m_D m_C and m_Z. The valence-band structure is calculated via the six-band Luttinger–Kohn Hamiltonian[13] for Si and Ge with common surface orientations—$\langle 100 \rangle$, $\langle 110 \rangle$, and $\langle 111 \rangle$—using a triangular-well approximation[14] and assuming an infinite potential barrier for the oxides at both interfaces of the semiconductors. In the following section, we will first consider the effect of coupling with the conduction band of type Γ_2^- and its implications on the use of a six-band Hamiltonian[13] description for band-structure calculation. Section III presents a brief outline of the numerical approach employed. In Sec. IV, we will provide an assessment of the energy quantization effect for the various surface orientations and its dependency on film thickness. Section V examines the energy anisotropy of the various Si and Ge thin films. Section VI concludes with a calculation of their 2D density of states.

[a]Electronic mail: elelimf@nus.edu.sg

TABLE I. Numerical values of bulk parameters used for the valence-band Hamiltonian for Si and Ge are obtained from Ref. 15. The Kane energy E_P, energy-gap E_G, and spin-orbit splitting Δ are given in units of eV. γ_j $(j=1,2,3)$ are Luttinger parameters and m_c is the effective mass (in units of free electron mass, m_0) at the band edge of type Γ_2^-, modified Luttinger parameter (not listed in table) for eight-band Hamiltonian can be calculated from Ref. 15.

	γ_1	γ_2	γ_3	E_G	Δ	E_P	m_c
Si	4.285	0.339	1.446	4.185	0.044	21.60	0.528
Ge	13.38	4.24	5.69	0.898	0.297	26.30	0.038

II. COUPLING WITH CONDUCTION BAND OF TYPE Γ_2^-

Calculating valence-band structure is complicated by the strong interaction between the various hole subbands. When T_{Body} is continuously scaled down, the hole quantization energy becomes comparable with the energy gap; therefore, possible coupling with the conduction bands should also be considered. In this work, we began with an eight-band Hamiltonian[15] description, including the valence-band coupling with the conduction band of type Γ_2^-, to investigate the sufficiency of a six-band Hamiltonian[13] approach with the parameters used listed on Table I. Figure 1 shows the comparison of hole subband structure calculated with an eight- and six-band Hamiltonian for both Si and Ge quantum wells with a $\langle 100\rangle$ surface and a T_{Body} of 30 Å. We observed that the hole subbands structure for Ge calculated with a six-band Hamiltonian deviates noticeably from the eight-band description, particularly for the higher subbands. From an analysis of the wave-function components for Ge subbands (see Fig. 2), it is evident that there is notable coupling with conduction band of type Γ_2^- for energy subband $n=2$, contributing to about 10% of the probability function. From this, we may conclude that an eight-band Hamiltonian approach is necessary for an accurate description of Ge hole subband structure.

For our work, however, a six-band Hamiltonian approach will suffice if the biasing condition is such that the hole carriers predominantly populate only the first subband of Ge; this usually applies to electrostatics under threshold condition. Our argument is as follows:

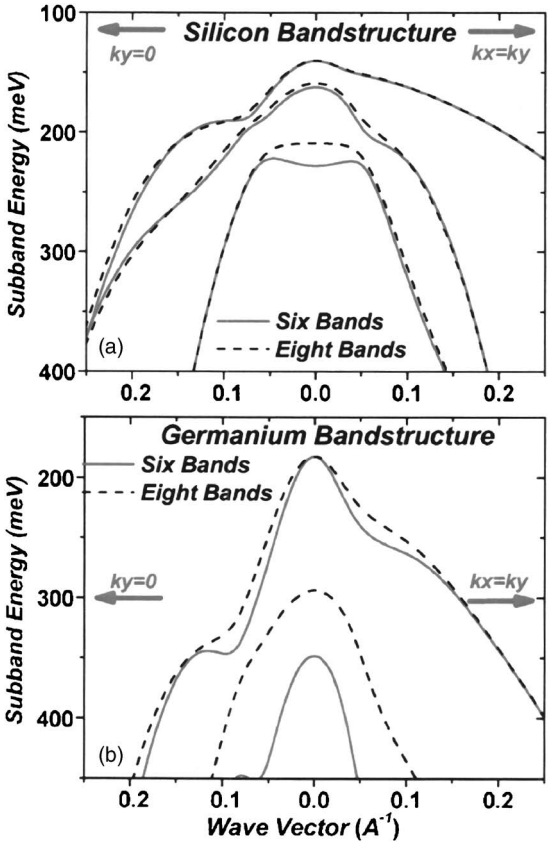

FIG. 1. Electronic hole subband structure for a 30-Å Si quantum well with $\langle 100\rangle$ surface with an infinite energy barrier height. Calculation is done with an eight-band (see Ref. 15) and six-band (see Ref. 13) Hamiltonian for comparison. Energy plotted along wave-vector direction of [010] and [110]. Confinement direction is taken to be along z.

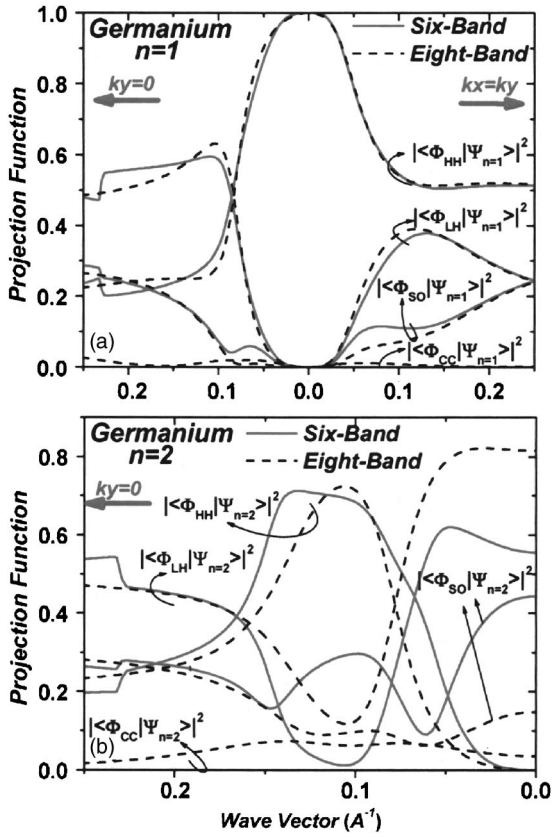

FIG. 2. Probability function projected on the various basis functions for 30-Å Ge quantum well with $\langle 100\rangle$ surfaces, plotted for energy level (a) $n=1$ and (b) $n=2$. Calculation is done with an eight-band (see Ref. 15) and six-band (see Ref. 13) Hamiltonian for comparison. $|\psi\rangle$ is the wave function for energy subband n and $|\phi_i\rangle$ $(i=\text{HH: heavy hole, LH: light hole, SO: split-off hole, and CC: conduction band of type } \Gamma_2^-)$ is the basis functions (Refs. 13 and 15) employed for our Hamiltonian.

(a) At threshold condition, the Fermi energy is approximately a few kT (~0.025 eV; k: Boltzmann's constant and T: temperature) away from the lowest subband energy minimum, where threshold condition is usually defined to be the onset of carrier inversion. Hence, higher hole subbands can be disregarded if they are a few kT higher than the lowest subband energy minimum.

(b) Ge generally has relatively small quantization masses, resulting in larger energy separations for the various subbands. In particular, for a 30-Å Ge quantum well with ⟨100⟩ surfaces, we have an energy separation (between $n=1$ and $n=2$) of ~0.1 eV.

Supported by these details, we shall adopt a six-band Hamiltonian approach in this work, exercising care when results pertaining to higher hole subbands of Ge are interpreted.

III. A NUMERICAL SOLUTION TO THE CHARGE CONTROL PROBLEM IN THE MOS SYSTEM

The numerical representation of the six-band Hamiltonian is obtained by following a discretization process outlined in Ref. 14. The six-band Hamiltonian is explicitly outlined in the Appendix where k_Z is represented by its differential form $-id/dz$ and coordinate z is taken to be the direction perpendicular to the semiconductor/oxide interface. When dealing with different crystal surface orientations of ⟨100⟩, ⟨110⟩, and ⟨111⟩, appropriate rotations of the **k** space must be performed. Although the charge control problem in the MOS system can be solved by obtaining the self-consistent solution to the Schrödinger and Poisson equations,[16] this approach is computationally intensive. In this work, we resort to the triangular-well approximation: $V(z)=eF_sz$, where F_S is the surface field and e the electronic charge. We must be aware of the limitations of the triangular-well approximation in describing MOS electrostatics under high inversion conditions,[16] where the charge-screening effect will alter the potential profile significantly. Despite this, the triangular approximation is computationally efficient and expected to be qualitatively correct, thus facilitating the study of a wider range of applications.

IV. IMPACT OF ACTIVE LAYER THICKNESS AND SURFACE ORIENTATION ON HOLE QUANTIZATION EFFECT

In this section, we will examine the effect of T_{Body} on the valence-band structure of Si and Ge with a sub-5-nm T_{Body}. In Fig. 3, hole subband energies (the lowest lying at $k=0$) are plotted as a function of T_{Body} for both Si and Ge channels with various surface orientations. At a high surface field of 1 MV/cm, the sub-band energies are generally less sensitive to the decrease of T_{Body} until a certain point ($T_{\text{Body}}\sim 4$ nm for $F_s=1$ MV/cm), where body quantization effects begin to be observed. We also noted that the energy quantization effect is strongest for ⟨100⟩ surface, followed by ⟨111⟩ and ⟨110⟩ surfaces.

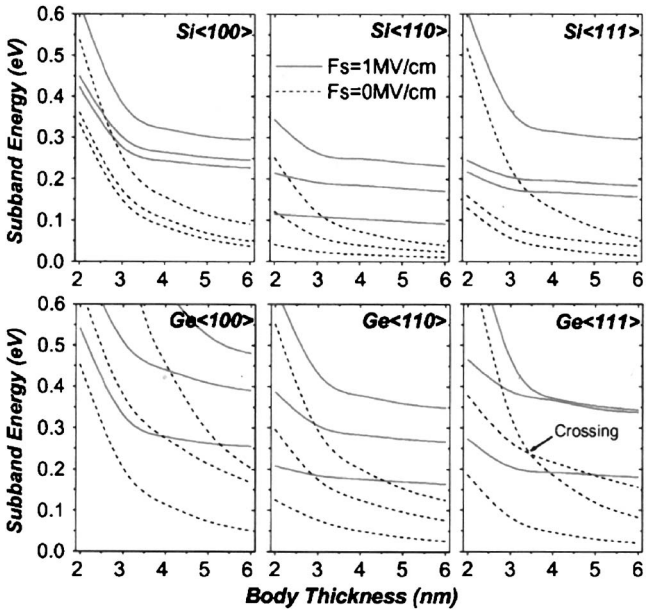

FIG. 3. Hole subband energies (at $\mathbf{k}=0$) as function of body thickness T_{Body}, plotted for (a) Si and (b) Ge channels with various surface orientations. Surface field Fs of 1 MV/cm (bold lines) and 0 MV/cm (dashed lines) are compared. For each case, only the lowest three subbands are shown. There is apparently a crossing of the second and third subband energy for Ge⟨111⟩ as T_{Body} is decreased.

It will be useful to provide a qualitative explanation for this observation. We begin by highlighting previous observations that the ground state of Si hole band structure are derived from the heavy-hole band.[17] Figure 4 shows the equienergy surface for the heavy-hole band of bulk Si, depicting the twelve distinct prongs. A particular crystal surface with prongs more aligned to the normal of the surface will effectively yield a larger "quantization mass." ⟨110⟩ surfaces have the prong perfectly aligned with the normal of the plane, which explains the small hole quantization effect on the ⟨110⟩ surface; this argument applies, with different results, for the ⟨100⟩ and ⟨111⟩ surfaces as well.

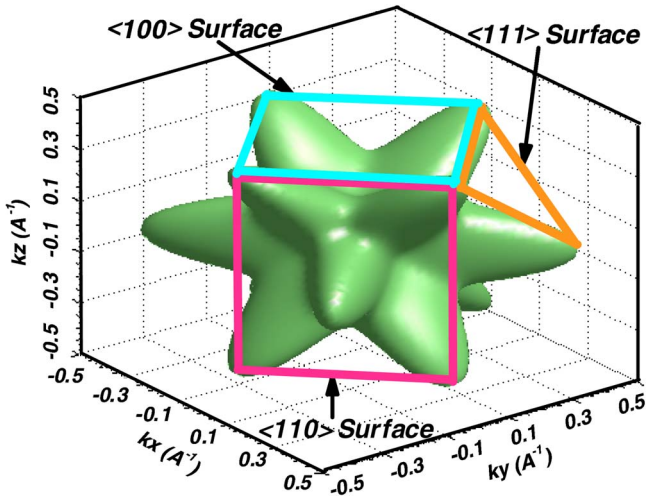

FIG. 4. Three-dimensional constant energy (at 0.1 eV reference from Γ point) surface plot for bulk Si band structure for the first valence energy band (or commonly known as heavy-hole band) depicting the twelve prominent *prongs*. The ⟨100⟩, ⟨110⟩, and ⟨111⟩ surface planes are illustrated and the axes are along [100] direction.

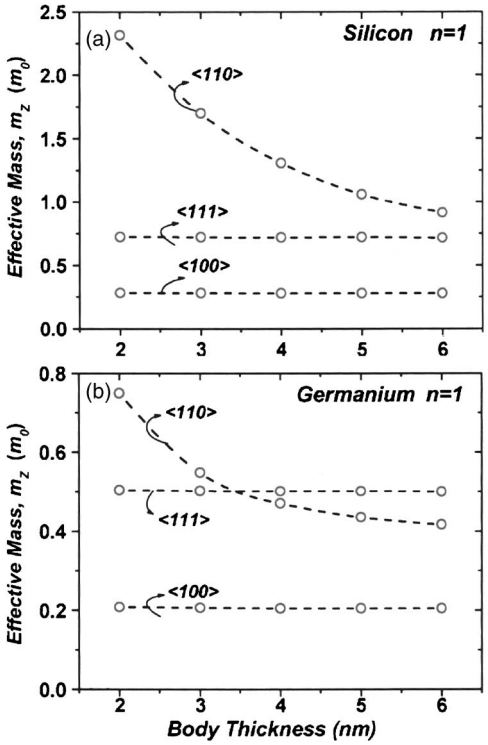

FIG. 5. Effective quantization mass m_2 calculated for (a) Si and (b) Ge quantum wells by fitting the subband energies at zone-center Γ to the analytical expression for that of a quantum well; $E_0=(\hbar^2/2m^*)(\pi/T_{\mathrm{BODY}})^2$.

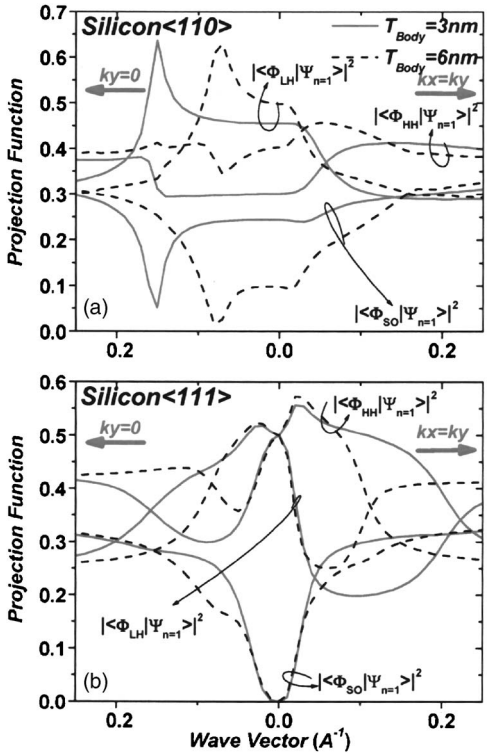

FIG. 6. Probability function projected on the various basis functions for 30 Å (bold line) and 60 Å (dashed line) Si quantum well, plotted for the first hole subband, with (a) ⟨110⟩ and (b) ⟨111⟩ surfaces. Calculation is done with a six-band (see Ref. 13) Hamiltonian. $|\psi_n\rangle$ is the wave function for energy subband n and $|\phi_i\rangle$ (i=HH: heavy hole, LH: light hole, and SO: split-off hole) is the basis functions (see Ref. 13) employed for our Hamiltonian.

Figure 5 computes the effective quantization mass (m_Z) for the ground-state subband in both the Si and Ge quantum wells under various surface orientations. This is calculated by fitting the subband energies at the zone-center Γ to the analytical expression for that of a quantum well with parabolic energy dispersion: $E_0=(\hbar^2/2m^*)(\pi/T_{\mathrm{BODY}})^2$. An interesting phenomenon—increasing effective quantization mass with decreasing T_{Body} for the ⟨110⟩ surface—is immediately revealed. The physical origin of this is the dependency of the valence-band mixing effect on the quantum well thickness. This effect can be analyzed by calculating the projection function, the probability function projected on the various basis functions employed for our Hamiltonian:[13] $|\Phi_i\rangle$ (i =HH: heavy hole, LH: light hole, and SO: split-off hole). Figure 6(a) illustrates the projection functions of the Si ⟨110⟩ quantum wells with a T_{Body} of 30 and 60 Å. Evidently, the projection function at Γ has a noticeable dependency on T_{Body}, revealing an increasing mix of split-off holes with decreasing T_{Body} around the vicinity of Γ. Conversely, the projection function in the vicinity of Γ for the ⟨100⟩ (Fig. 2) and ⟨111⟩ [Fig. 6(b)] surfaces does not exhibit such anomalous characteristics. Thus, we may conclude that their m_Z are independent of T_{Body} (Si⟨100⟩$\sim 0.28m_0$, Si⟨111⟩$\sim 0.72m_0$, Ge⟨100⟩$\sim 0.21m_0$, and Ge⟨111⟩$\sim 0.50m_0$).

V. ENERGY DISPERSION AND ANISOTROPY

Anisotropic energy dispersion and its effect on transport anisotropy in Si MOSFETs have been investigated theoretically.[14] There are also experimental studies of its transport characteristics in both the low-field[18,19] and high-field regime.[20] However, a study of hole energy dispersion anisotropy and its dependency on film thickness have not yet been conducted. Energy dispersion for the first two hole subbands of Si (Fig. 7) and Ge (Fig. 8) are plotted for two particular conditions as follows: (i) Bulk F_s=1 MV/cm and T_{Body}=100 nm, shown on the right and (ii) UTB F_s =1 MV/cm and T_{Body}=3 nm, shown on the left. Of particular interest are the following observations:

(1) ⟨100⟩ surface orientation: The energy dispersion characteristics of Si⟨100⟩ for both bulk and UTB devices [as depicted in Fig. 7(a)] look similar except with a larger uplift of the n=2 subband for the UTB device due to the body quantization effect. The ground-state energy (n =1) for Si⟨100⟩ maintains its strong anisotropy with the decrease of T_{Body} to 3 nm, presenting an optimum channel direction (smallest m_C along [100] as elucidated in Figs. 7(a) and 9(a). The n=2 subband presents an apparent optimum channel direction along [110]. The anisotropy of the two subbands may neutralize each other, rendering the observed transport characteristics relatively isotropic. This is, in fact, the experimental observation for bulk Si MOSFETs.[19] However, the increased body quantization effect in UTB MOSFETs will result in carrier occupation dominance of the ground-state energy and it is very likely that the current anisotropy characteristics, due to the n=1 subband may ultimately manifest. For Ge⟨100⟩, it is noted in Fig. 9(b) that its energy anisotropy is less severe than Si⟨100⟩, with a significant

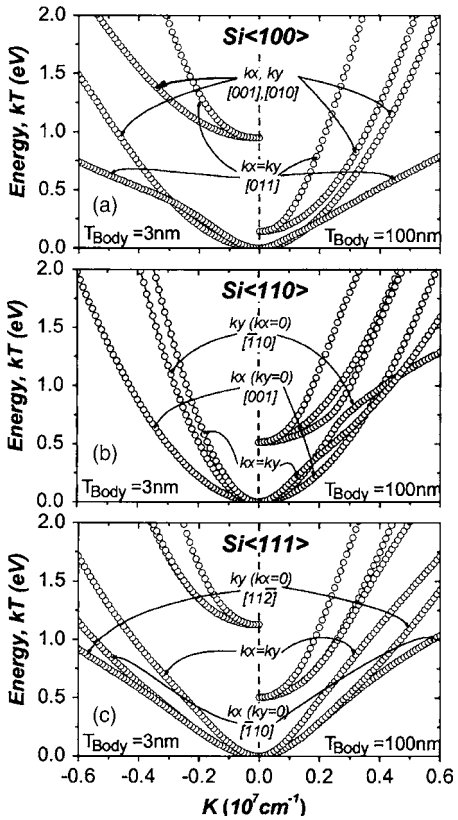

FIG. 7. Energy dispersion of Si (sub-band E_1 and subband E_2) plotted at surface field F_S=1 MV/cm for T_{Body}=100 nm (right) and T_{Body}=3 nm (left). For ⟨100⟩ and ⟨110⟩ surface, k_X is parallel to [001] channel direction. For ⟨111⟩ surface, k_X is parallel to [110] direction.

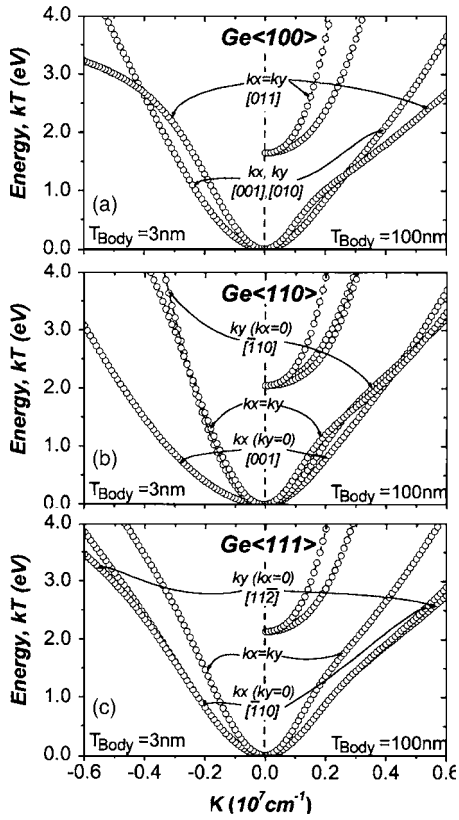

FIG. 8. Energy dispersion of Ge (subband E_1 and subband E_2) plotted at surface field F_S=1 MV/cm for T_{Body}=100 nm (right) and T_{Body}=3 nm (left). For ⟨100⟩ and ⟨110⟩ surface, k_X is parallel to [001] channel direction. For ⟨111⟩ surface, k_X is parallel to [110] direction. E_2 subband energy for T_{Body}=3 nm is too high to be shown in the figure.

relaxation of the energy anisotropy of ground-state energy as T_{Body} is decreased.

(2) ⟨110⟩ surface orientation: In Sec. IV, we noted the dependency of the valence-band mixing effect on the quantum well thickness for ⟨110⟩ surface thin film and its effect on m_Z. It can be anticipated that this dependency of valence-band mixing effect on the quantum well thickness will also have an important effect on the energy dispersion characteristics for the ⟨110⟩ surface. Figures 7(b) and 8(b) depict a notable change in the energy dispersion of the $n=1$ subband for Si⟨110⟩ and Ge⟨110⟩, respectively, as the T_{Body} is decreased to 3 nm. Specifically, this change is an increase of the energy gradient drawn along the k_y (at $k_x=0$, this is the [011] channel direction) and $k_x=k_y$ directions. The main effect of this will be in its carrier velocity, as elucidated in Fig. 10, which plots the radial carrier velocity $[\mathbf{v}(\mathbf{k})=\hbar^{-1}\partial\mathbf{E}/\partial\mathbf{k}$ where the energy derivative is taken along the radial direction] of $n=1$ subband for both the (a) bulk and (b) UTB devices. A significantly higher intensity for carrier velocity is observed in the UTB device than in its bulk counterpart. Recently, it was experimentally observed that the optimum low-field mobility direction for Si UTB devices with a ⟨110⟩ surface is along the [011] channel direction (see Fig. 11 of Ref. 14). For Si⟨110⟩ bulk MOSFETs, it was also experimentally found that the anisotropy characteristic of low-field mobility is not significant.[18] These experimental observations correlate with our theoretical calculations and should also qualitatively apply to Ge⟨110⟩ since its energy dispersion characteristics are similar to Si⟨110⟩.

VI. IMPACT OF SURFACE ORIENTATION ON DENSITY OF STATES

Figure 11 plots the 2D density of states for Si and Ge thin films with a T_{Body} of 3 nm. Density of states for Ge are several times smaller than for its Si counterpart, with the ⟨110⟩ surface having the smallest density of states, followed by the ⟨111⟩ and then ⟨100⟩. From a density-of-states point of view, the employment of Ge⟨110⟩ crystal for the device's active layer will be helpful in achieving a high-mobility channel.

VII. CONCLUSIONS

In summary, our examination of the impact of film thickness on the hole subband structure of Si and Ge thin films within the framework of *kp* approximation via the Luttinger–Kohn Hamiltonian has shown an anomalous increase of "effective quantization mass" for the ⟨110⟩ surface as T_{Body} is decreased. This phenomenon is due to the body-thickness-dependent valence-band mixing effect in vicinity of the zone-center Γ. The other two orientations exhibit relatively constant effective quantization mass as T_{Body} is decreased, with Ge having a consistently smaller effective quantization

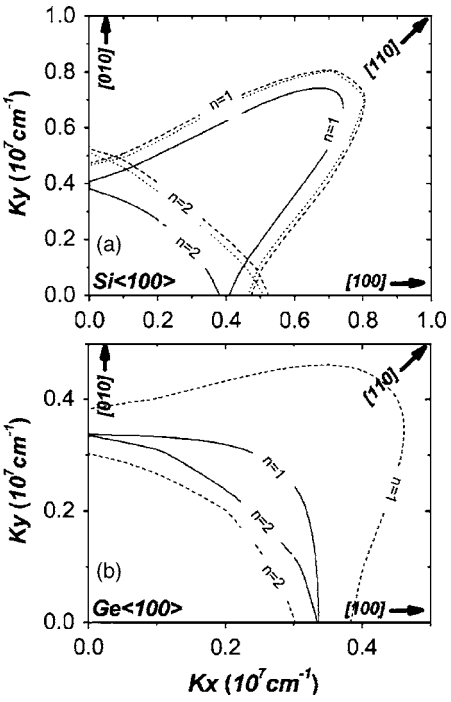

FIG. 9. Equienergy lines for the first two hole subbands of (a) Si⟨100⟩ and (b) Ge⟨100⟩ plotted at energy $(E-E_i, i=1,2)$ of 25, and 50 meV, respectively, under (i) bulk high-field conditions: $F_S=1$ MV/cm and $T_{\mathrm{Body}}=100$ nm, represented by solid lines and (ii) UTB high-field conditions: $F_S=1$ MV/cm and $T_{\mathrm{Body}}=3$ nm, represented by dashed lines.

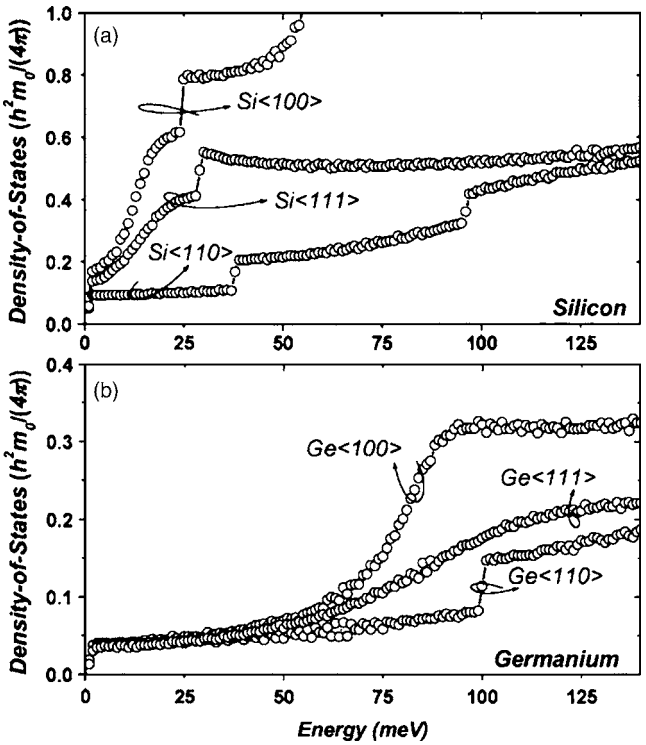

FIG. 11. Density of states for (a) Si and (b) Ge quantum wells for a particular spin state at $F_S \sim 0.1$ MV/cm and $T_{\mathrm{Body}}=3$ nm. Contributions from all the subbands are summed.

mass than its Si counterpart. It has also been observed that energy dispersion anisotropy exhibits a dependence on film thickness, especially for the ⟨110⟩ surface. In particular, its radial carrier velocity along the [011] channel increases as the T_{Body} is decreased. Calculated density of states of Ge thin film are several times smaller than its Si counterpart, indicating that Ge should prove advantageous for the implementation of high-mobility channels. These findings should provide useful guidelines for the design of UTB *p*-MOSFETs.

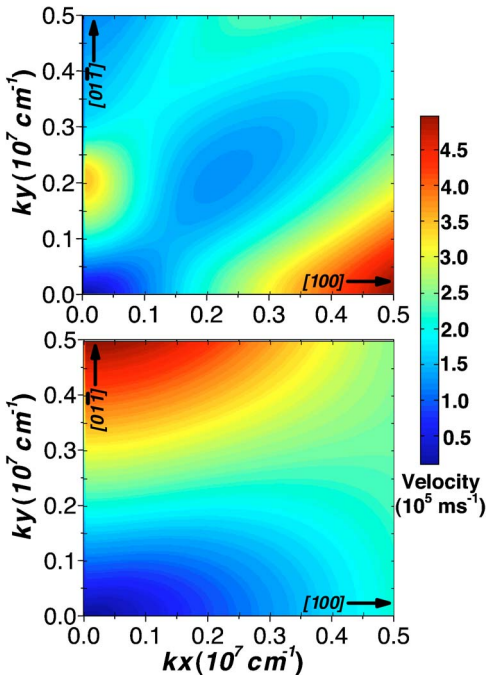

FIG. 10. Intensity plot for hole carrier radial velocity of different in-plane wave vector. Plotted for the ground-state energy of Si⟨110⟩ for (a) $T_{\mathrm{Body}}=100$ nm and (b) $T_{\mathrm{Body}}=3$ nm at $F_S=1$ MV/cm. Radial velocity $\boldsymbol{v}(\boldsymbol{k})=\hbar^{-1}\partial \boldsymbol{E}/\partial \boldsymbol{k}$, is obtained by taking the gradient of its energy dispersion in the radial direction.

ACKNOWLEDGMENTS

This work is supported by the Singapore A*STAR R263-000-267-305 and IME/03-450002 JML/SOI Grants. One of the authors (T.L.) gratefully acknowledges the scholarships from Singapore Millennium Foundation and Chartered Semiconductor Manufacturing.

APPENDIX

The basis functions employed for Kohn–Luttinger Hamiltonian[13] are depicted as follows:

$$\left|\frac{3}{2},\frac{3}{2}\right\rangle = \frac{1}{\sqrt{2}}|x\rangle\uparrow + \frac{1}{\sqrt{2}}|y\rangle\uparrow,$$

$$\left|\frac{3}{2},\frac{1}{2}\right\rangle = i\frac{1}{\sqrt{6}}|x\rangle\downarrow - \frac{1}{\sqrt{6}}|y\rangle\downarrow - i\frac{\sqrt{2}}{\sqrt{3}}|z\rangle\uparrow,$$

$$\left|\frac{3}{2},-\frac{1}{2}\right\rangle = \frac{1}{\sqrt{6}}|x\rangle\uparrow - i\frac{1}{\sqrt{6}}|y\rangle\uparrow + \frac{\sqrt{2}}{\sqrt{3}}|z\rangle\downarrow,$$

$$\left|\frac{3}{2},-\frac{3}{2}\right\rangle = i\frac{1}{\sqrt{2}}|x\rangle\downarrow + \frac{1}{\sqrt{2}}|y\rangle\downarrow,$$

$$\left|\frac{1}{2},\frac{1}{2}\right\rangle = \frac{1}{\sqrt{3}}|x\rangle\downarrow + i\frac{1}{\sqrt{3}}|y\rangle\downarrow + \frac{1}{\sqrt{3}}|z\rangle\uparrow,$$

$$\left|\frac{1}{2},-\frac{1}{2}\right\rangle = -i\frac{1}{\sqrt{3}}|x\rangle\uparrow - \frac{1}{\sqrt{3}}|y\rangle\uparrow + i\frac{1}{\sqrt{3}}|z\rangle\downarrow.$$

Where the functions $|X\rangle$, $|Y\rangle$, and $|Z\rangle$ are the basis functions of Γ_4 representation of the tetrahedral point group. The above choice of basis functions allows us to diagonalize the well-known spin-orbit coupling term, H_{SO} [see for, e.g., Ref. 13 eq. (V.1)]. Hence the Kohn–Luttinger Hamiltonian is

$$\begin{bmatrix} \mathrm{HH} & \alpha & \beta & 0 & \frac{i\alpha}{\sqrt{2}} & -i\sqrt{2}\beta \\ \alpha^* & \mathrm{LH} & 0 & \beta & \kappa & i\frac{\sqrt{3}}{\sqrt{2}}\alpha \\ \beta^* & 0 & \mathrm{LH} & -\alpha & -i\frac{\sqrt{3}}{\sqrt{2}}\alpha^* & \kappa \\ 0 & \beta^* & -\alpha^* & \mathrm{HH} & -i\sqrt{2}\beta^* & -\frac{i\alpha}{\sqrt{2}} \\ \frac{i\alpha^*}{\sqrt{2}} & \kappa^* & i\frac{\sqrt{3}}{\sqrt{2}}\alpha & i\sqrt{2}\beta & \mathrm{SO}-\lambda & 0 \\ i\sqrt{2}\beta^* & -i\frac{\sqrt{3}}{\sqrt{2}}\alpha^* & \kappa^* & \frac{i\alpha}{\sqrt{2}} & 0 & \mathrm{SO}-\lambda \end{bmatrix},$$

where:

$$\mathrm{HH} \equiv \frac{h^2}{2m}[(\gamma_1+\gamma_2)(k_x^2+k_y^2)+(\gamma_1-2\gamma_2)(k_z^2)],$$

$$\mathrm{LH} = \frac{h^2}{2m}[(\gamma_1-\gamma_2)(k_x^2+k_y^2)+(\gamma_1+2\gamma_2)k_z^2],$$

$$\mathrm{so} = \frac{h^2}{2m}[\gamma_1(k_x^2+k_y^2+k_z^2)],$$

$$\alpha \equiv \frac{h^2}{2m}[-i2\sqrt{3}\gamma_3(k_x-ik_y)k_z],$$

$$\beta \equiv \frac{h^2}{2m}[\sqrt{3}\gamma_2(k_x^2-k_y^2)-i2\sqrt{3}\gamma_3 k_x k_y],$$

$$\kappa \equiv \frac{h^2}{2m}i\sqrt{2}\gamma_2[-(k_x^2+k_y^2)+2k_z^2],$$

where λ is the spin-orbit splitting.

For $\langle 110\rangle$ surface, a rotation of the original **k** space is required:

$$k_x' = k_x,$$

$$k_y' = \frac{1}{\sqrt{2}}k_y + \frac{1}{\sqrt{2}}k_z,$$

$$k_z' = -\frac{1}{\sqrt{2}}k_y + \frac{1}{\sqrt{2}}k_z,$$

and similarly for $\langle 111\rangle$ surface:

$$k_x' = \sqrt{\frac{2}{3}}k_x - \frac{1}{\sqrt{6}}k_y + \frac{1}{\sqrt{6}}k_z,$$

$$k_y' = \frac{1}{\sqrt{2}}k_y + \frac{1}{\sqrt{2}}k_z,$$

$$k_z' = -\frac{1}{\sqrt{3}}k_x - \frac{1}{\sqrt{3}}k_y + \frac{1}{\sqrt{3}}k_z.$$

[1] D. Edenfeld, A. B. Kahng, M. Rodgers, and Y. Zorian, *2003 International Technology Roadmap for Semiconductors* (IEEE Computer Society, California, 2004).

[2] K. Uchida, H. Watanabe, A. Kinoshita, J. Koga, T. Numata, and S. Takagi, *International Electron Devices Meeting*, San Francisco, CA, 8–11 December 2002 (IEEE, New York, 2002), p. 47.

[3] K. Uchida and S. Takagi, Appl. Phys. Lett. **82**, 2916 (2003).

[4] This experimental observation is first reported in Ref. 2 for a Si *n*-MOSFETs, done at low vertical electric-field condition of 0.1 MV/cm at 25 K.

[5] H. Sakaki, T. Noda, K. Hirakawa, M. Tanaka, and T. Matsusue, Appl. Phys. Lett. **51**, 1934 (1987).

[6] M. S. Lundstrom, IEEE Electron Device Lett. **22**, 293 (2001).

[7] The physical mechanism for the drastic degradation of mobility is identified to be due to surface roughness (SR) related scattering mechanisms via a low-field mobility measurement at 25 K (Refs. 2 and 3). In addition, the electron mobility follows a T_{Body} to-power-of-six relationship (Ref. 4), which has also been observed in quantum well structures (see Ref. 5). Lundstrom has pointed out (Ref. 6), via a phenomenological approach, that the steady-state current in a decananometer MOSFETs is essentially source limited, although scattering processes at the drain side may affect the transport potential profile via the self-consistency loop. Hence the mobility at high vertical surface field, which embodies the effective scattering rate in vicinity of the source, remains relevant. Consider the electron at the source with carrier velocity of 1×10^5 m/s with an effective momentum relaxation time of 1×10^{-14} s, this yields a mean free path of merely 1 nm. SR scattering in aggressively scaled T_{Body} will further shorten the effective momentum relaxation time.

[8] T. Tezuka, S. Nakaharai, Y. Moriyama, N. Sugiyama, and S. Takagi, *Symposium on VLSI Technology*, Honolulu, HI, 15–17 June 2004 (IEEE, New York, 2004), p. 198.

[9] M. Yang *et al.*, *International Electron Devices Meeting*, Washington, DC, 8–10 December 2003 (IEEE, New York, 2003), p. 453.

[10] T. Low, M. F. Li, C. Shen, Y. C. Yeo, Y. T. Hou, C. Zhu, A. Chin, and D. L. Kwong, Appl. Phys. Lett. **85**, 2402 (2004).

[11] T. Low, Y. T. Hou, M. F. Li, C. Zhu, A. Chin, G. Samudra, L. Chan, and D. L. Kwong, *International Electron Devices Meeting*, Washington, DC, 8–10 December 2003 (IEEE, New York, 2003), p. 691.

[12] T. Low, Chen Shen, M. F. Li, Y. C. Yeo, Y. T. Hou, C. Zhu, A. Chin, L. Chan, and D. L. Kwong, *Study of Mobility in Strained Si and Ge Ultrathin-Body MOSFETs* (SSDM, Tokyo, 2004), p. 776.

[13] J. M. Luttinger and W. Kohn, Phys. Rev. **97**, 869 (1955).

[14] M. V. Fischetti, Z. Ren, P. M. Solomon, M. Yang, and K. Rim, J. Appl. Phys. **94**, 1079 (2003).

[15] S. Ridene, K. Boujdaria, H. Bouchriha, and G. Fishman, Phys. Rev. B **64**, 085329 (2001).

[16] T. Low, Y. T. Hou, and M. F. Li, IEEE Trans. Electron Devices **50**, 1284 (2003).

[17] See Ref. 14. The nature of each sub-band was established by analyzing the shape of the equienergy lines in **k** space and by counting the nodes of the wave function. It is found that the ground state is always heavy-holelike

under a triangular potential well over a surface field range from 0 to 2.5 MV/cm.
[18]T. Sato, Y. Takeishi, H. Hara, and Y. Okamoto, Phys. Rev. B **4**, 1950 (1971).
[19]T. Sato, Y. Takeishi, and H. Hara, Jpn. J. Appl. Phys. **8**, 588 (1969).
[20]M. Kinugawa, M. Kakumu, T. Usami, and J. Matsunaga, *International Electron Devices Meeting*, Washington, DC, 5–8 December 1985 (IEEE, New York, 1985) p. 581.